Journal of Alloys and Compounds 934 (2023) 167759

Contents lists available at ScienceDirect

Journal of Alloys and Compounds

journal homepage: www.elsevier.com/locate/jalcom

Mechanical and electrical properties of Cu30Cr0.2Zr composites enhanced by CeO_2/GO

Shengli Liang [a,1], Yunzhang Li [a,*], Yi Zhang [a,b,c,**], Meng Zhou [a,b,c,**], Shuang Liu [a,1], Xu Li [d], Yongfeng Geng [e], Baohong Tian [a,b,c], Yanlin Jia [f], Yong Liu [a,b,c], Alex A. Volinsky [g]

[a] School of Materials Science and Engineering, Henan University of Science and Technology, Luoyang 471023, PR China
[b] Provincial and Ministerial Co-construction of Collaborative Innovation Center for Non-ferrous Metal new Materials and Advanced Processing Technology, Henan Province, Luoyang 471023, PR China
[c] Henan Province Key Laboratory of Nonferrous Materials Science and Processing Technology, Luoyang 471023, PR China
[d] Center for Advanced Measurement Science, National Institute of Metrology, Beijing 100029, PR China
[e] State Key Laboratory of Metal Matrix Composites, Shanghai Jiao Tong University, Shanghai 200240, China
[f] College of Materials Science and Engineering, Central South University, Changsha 410083, China
[g] Department of Mechanical Engineering, University of South Florida, Tampa 33620, USA

ARTICLE INFO

Article history:
Received 2 May 2022
Received in revised form 5 October 2022
Accepted 25 October 2022
Available online 27 October 2022

Keywords:
CeO_2/GO
In-situ formation
Interface
Mechanical properties
Electrical properties

ABSTRACT

The interface structure of Cu30Cr0.2Zr electrical contacts was modified using CeO_2/GO to improve the mechanical properties and obtain good arc erosion resistance. A small amount of $Cr_{23}C_6$ nanoparticles and Cr_3C_2 carbide layer were formed in situ at the rGO-CuCrZr interface, and $Cu_{10}Zr_7$ nanoparticles were formed in the CuCrZr matrix, which significantly improved the interfacial adhesion of the composites. CeO_2/GO increased the Cu30Cr0.2Zr composites tensile strength from 276 MPa to 406 MPa, and the elongation at failure increased threefold. The strength enhancement was ascribed to the load transfer effect of graphene and the dual effect of interfacial bonding. While the strength was improved, the conductivity increased by more than 30%, which is attributed to the dual action of the high conductivity of rGO (reduced graphene oxide) and ionic CeO_2. At the same time, CeO_2/GO dispersed the electrode arc, alleviated the concentrated erosion of the arc, weakened the loss of Cu30Cr0.2Zr electrode material, improved the welding resistance, and reduced the energy of arc burning. In addition, it had good thermal conductivity, reduced the formation of erosion pits and thermal cracks, and prolonged the service life of the electrode. This study provides a strategy for developing copper-based electrical contact composites with a good combination of strength, ductility, and electrical conductivity.

1. Introduction

Copper matrix composites have excellent mechanical strength, weldability, dimensional stability, and excellent electrical conductivity [1]. Electrical contact materials must have adequate electrical and mechanical properties, along with long-term stability. They are used for current transfer in many technologies, including artificial intelligence, automotive industry, and military applications [2–6]. During making and breaking electrical contacts in the control circuit, high-energy arc discharge can occur in the contact gap, resulting in contact erosion and welding. If serious, the service life of paired electrical contacts will be shortened or they can even fail [7–9]. Therefore, it is very important to design new types of electrical contact materials with arc resistance and good welding performance, which can ensure reliable and smooth operation of the circuit.

Previous studies have shown that the comprehensive properties of copper matrix composites can be greatly improved by adding appropriate reinforcing agents. The conventional design strategy of electrical contact materials is to disperse conventional particle reinforcers such as carbides (SiC, WC) [6,10], oxide ceramics (Al_2O_3, SiO_2) [11,12], and nitrous compounds (BN) [13] in the metal matrix. Such reinforcers

* Corresponding author.
** Corresponding authors at: School of Materials Science and Engineering, Henan University of Science and Technology, Luoyang 471023, PR China
E-mail addresses: liyunzhang95@163.com (Y. Li), yizhang@haust.edu.cn (Y. Zhang), zhoumeng0902@126.com (M. Zhou).
[1] These authors contributed equally to this work.

https://doi.org/10.1016/j.jallcom.2022.167759
0925-8388/

enhance the mechanical strength, but due to their weak electrical and thermal properties, they sacrifice electrical and thermal conductivity of copper matrix composites. Moreover, the arc is preferentially generated on the matrix surface and is continuously reignited on the particles of the discontinuous reinforcer, resulting in arc concentrated erosion and deterioration of the electrical contact surface [14,15]. The reinforcement with continuous structures improves mechanical and thermophysical properties, disperses the arc, and reduces arc erosion by directing arc movement, thus extending the service life of electrical contacts and the entire electrical system [16,17].

Graphene has high electrical and thermal conductivity, extraordinary intrinsic mobility, high fracture strength (130 GPa), Young's modulus (1 TPa), and a low density (2.2 g/cm^3) [18–23], which make it an ideal potential reinforcement for copper matrix composites. Using graphene as reinforcement is expected to overcome the degradation of copper matrix composites' electrical properties caused by reinforcement materials such as ceramic particles [24,25]. However, the weak interfacial bond between graphene and Cu matrix, high static power, and van der Waals forces lead to the accumulation and agglomeration of graphene in the matrix, their homogeneous distribution within the composites is thus extremely difficult to be achieved by traditional mixing methods [26,27]. This presents a challenge to the applications of two-dimensional graphene as matrix reinforcement.

In order to obtain high-performance graphene-copper matrix composites, many efforts have been made to promote the dispersion of graphene and enhance interfacial bonding. One possible approach is to use graphene derivatives, such as graphene oxide (GO), to increase interfacial wettability. The rich functional groups on GO provide binding sites for interfacial bonding. However, the loss of some functional groups at high temperatures degrades graphene's extraordinary properties [28,29]. Zhang et al. [7] prepared GO-reinforced Al_2O_3-Cu/35W5Cr composite by freeze-drying and discharge plasma sintering, which has 403 MPa ultimate tensile strength and 68.4% IACS electrical conductivity. Another possible solution is to add a transition layer between graphene and the matrix to ensure efficient heat and load transfer [30]. Chu et al. [31] investigated the CuCr strengthening mechanism enhanced by graphene and found that trace Cr_7C_3 layers/nanoparticles were formed in situ at the rGO-CuCr interface, which significantly improved the interfacial bonding and mechanical properties of composites. Liu et al. [32] reported improved interfacial bonding and thermal conductivity of TiC and Mo_2C coated graphite fiber-reinforced copper matrix composites. In addition, graphene encapsulation-powder consolidation is also an effective way to obtain high-performance graphene-metal composites. Zhang et al. [33] used the method of ambient-pressure rapid thermal annealing to rapidly grow graphene-like nanosheets (GLNs) in situ on Cu powder. The 3D-GLNN network is then built in- situ during the hot-pressing process, while the Cu powder is rapidly densified. 3D-GLNN not only imparts a much greater interfacial shear stress than 2D isolated graphene in the composite, resulting in better load transfer enhancement capability and significantly higher enhancement efficiency, but also greatly reduces the scattering of electrons in the interface region and constructs a wide range of electron transmission conductive channels throughout the matrix.

The wettability of graphene derivatives and the matrix, along with the addition of carbide elements are effective ways to optimize the comprehensive properties of graphene-reinforced copper matrix composites. In this work, the hydrothermal method was used to modify the surface of GO, which improved the dispersion uniformity of graphene in the matrix, and reduced contact damage. Adding Cr also improved the interfacial bond strength. The interface microstructure evolution and mechanical properties enhanced by graphene are analyzed and discussed in this paper. The mechanisms of mechanical and electrical contact properties improvement by graphene in copper matrix composites are outlined.

2. Materials and methods

GO was prepared from natural flake graphite by the improved Hummers' method [34,35]. CeO_2/GO nanocomposites were prepared by the hydrothermal method [36], shown schematically in Fig. 1. The obtained end products were dispersed in deionized water and treated in an ultrasonic bath for 30 min. Mixed metal powder

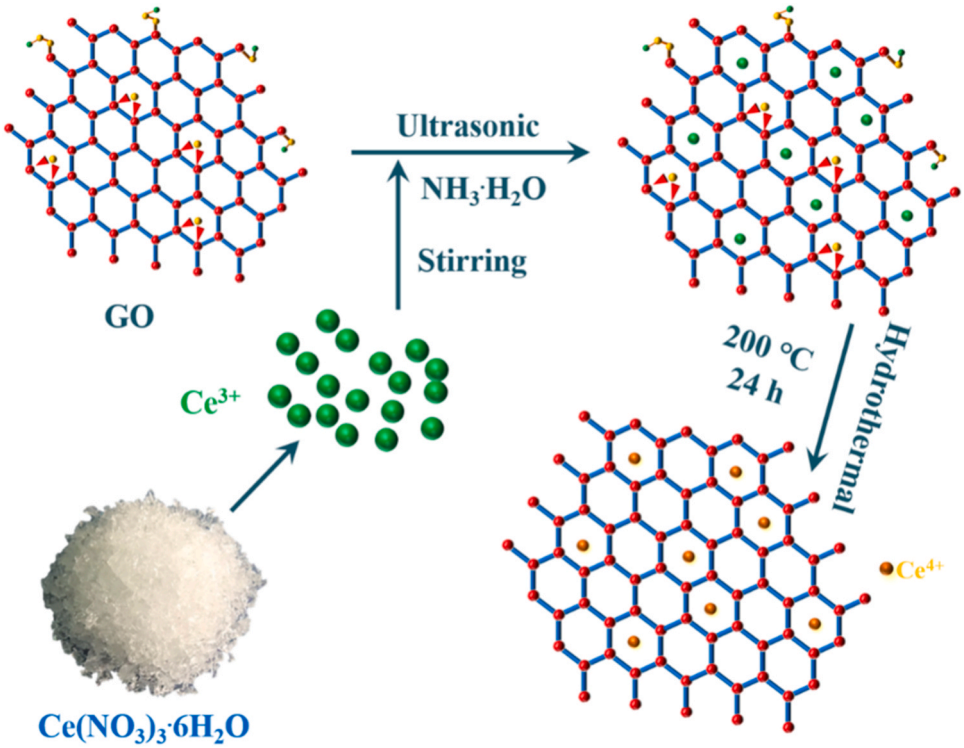

Fig. 1. Schematics of the CeO_2/GO nanocomposites preparation process.

containing pure Cu powder (5 μm average diameter), Cr powder (47 μm average particle size), and Zr powder (25 μm average diameter), was transferred to CeO_2/GO nanocomposites suspension after ultrasonic treatment, mechanically stirred for 6 h and dried in a vacuum freeze dryer for 72 h. Using pure Cu balls (10:1 ball/material ratio) as the grinding medium, the mixed powder was ground in a Y-type mixer at 50 rpm for 4 h. The samples were sintered for 8 min in the SPS furnace at 950 °C (100 °C/min heating rate) and 50 MPa pressure. In order to evenly heat the sample, the sintering temperature was held for 5 min, after which 50 MPa pressure was applied.

X-ray diffraction (XRD) and Raman spectroscopy were used to characterize the structure of GO and CeO_2/GO nanocomposites. The relative density of sintered samples was measured by the Archimedes method using deionized water as the medium. The electrical and thermal conductivity of the composites was evaluated by the Sigma 2018B1 eddy current conductivity meter and DIL 402SE thermal conductivity tester, respectively. The structure and reduction degree of GO were obtained by X-ray photoelectron spectroscopy (XPS). The microstructure and morphology of the samples were characterized by transmission electron microscopy (TEM), electron backscatter diffraction (EBSD), and scanning electron microscopy (SEM). The uniaxial tensile tests were carried out at room temperature using the AG-I 250 KN universal testing machine with a constant deformation rate of 1 mm/min. Three samples of each composite were tested repeatedly to verify the test accuracy and repeatability. In the electrical contact test, the moving contact was used as the anode and the static contact was used as the cathode. Each contact pair was tested 5000 times in the JF04C electrical contact test system. The applied voltage was 25 V DC, the current was 10 A, 20 A, 25 A, and 30 A, and the contact pressure was 0.4–0.6 N.

3. Results

3.1. Structure and morphology of GO and CeO_2/GO nanocomposites

In order to understand the crystallographic structure of the obtained samples, XRD and Raman spectra of the synthesized GO and

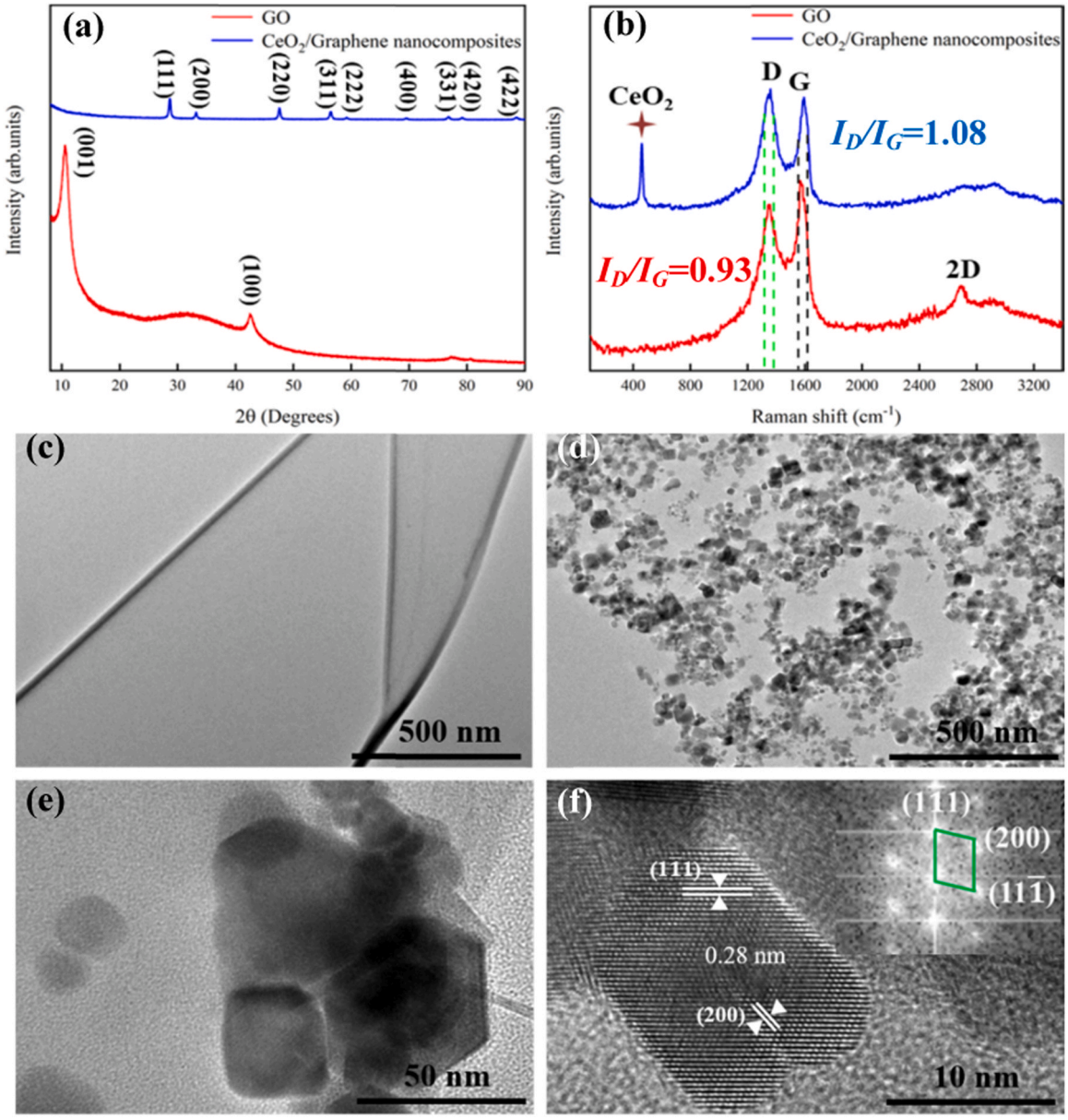

Fig. 2. Structure and morphology of GO and CeO_2/GO: (a) XRD and (b) Raman spectra; (c-e) TEM images of GO and CeO_2/GO; (f) HRTEM images of CeO_2 nanoparticles in graphene nanocomposites.

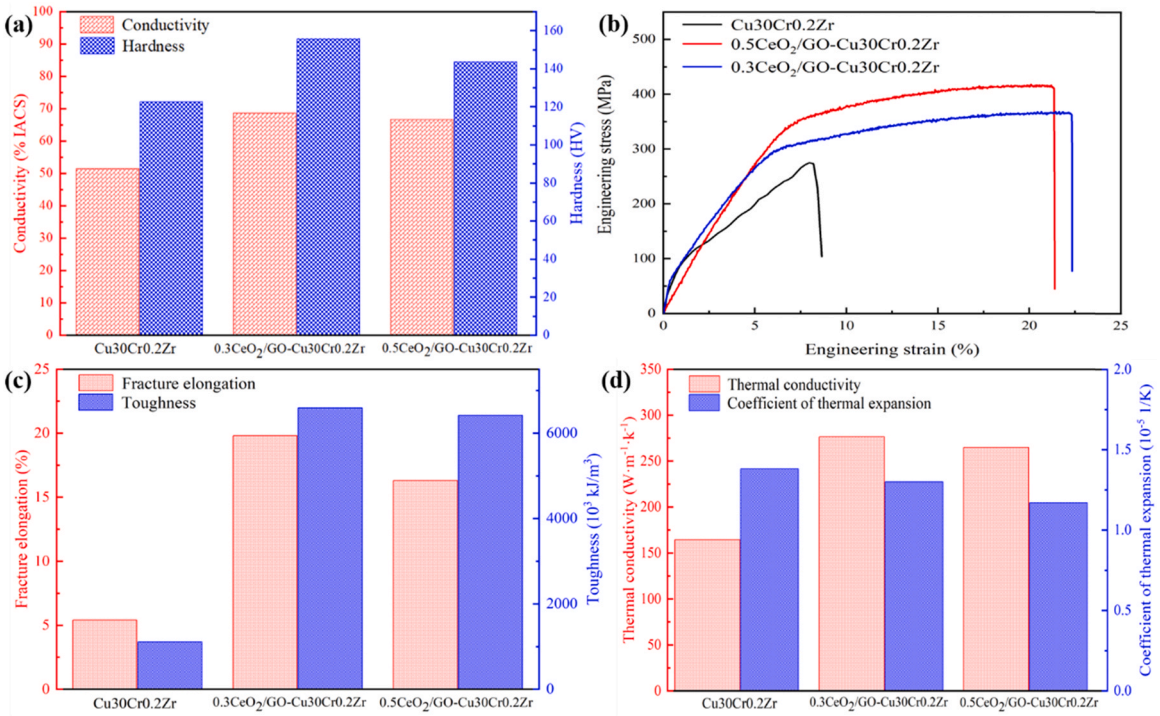

Fig. 3. Comprehensive properties of three composite materials: (a) Conductivity and hardness; (b) Engineering stress-strain curves; (c) Bar graph of fracture elongation and toughness; (d) Bar chart of thermal properties.

CeO_2/GO samples were measured. The obtained spectra are shown in Fig. 2(a, b). In the diffraction pattern of GO, typical diffraction reflection from the (100) crystal planes appear at 10.6°, corresponding to d= 0.833 nm, which is significantly larger than the natural graphite (d=0.334 nm). This is because after strong oxidation of natural graphite, oxygen-containing groups are formed on both sides of the GO sheet, resulting in structural defects (sp^3) on the flat sheet, and higher roughness at the atomic scale. The XRD pattern of CeO_2/GO shows CeO_2 nanocubes with typical fluorite structure, and the main reflections of the (111), (200), (220), (311), (222), (400), (331), (420) and (422) planes are consistent with CeO_2 (PDF#34–0394), indicating that the obtained CeO_2 nanocrystals have high crystallinity. In addition, only a very weak diffraction reflection of GO was observed in the spectra, indicating that GO was reduced under hydrothermal action and mainly contained single or several layers of graphene products. These results are consistent with Raman and TEM results. Raman spectroscopy is a convenient and nonvolatile technique for the characterization of graphite materials. Fig. 2(b) shows the Raman spectra of GO and CeO_2/GO. The 1.08 D/G intensity ratio of the loaded nanocomposites is higher than GO (0.93), while the D and G peaks are slightly red-shifted. This change indicates that the amount of GO is decreasing and there is charge transfer between CeO_2 and GO nanosheets. In addition, another obvious peak at 461.15 cm^{-1} belongs to the Raman activity spectra of the O-Ce-O symmetrical stretching vibration F_{2g} mode of CeO_2 particles [37]. At the same time, it also shows that CeO_2 nanoparticles are well riveted on the surface of graphene products.

Fig. 2(c-f) show the TEM images of the GO sheet and CeO_2/GO, respectively. The GO sheet is colorless and transparent, and the edge has visible folds. A large number of CeO_2 nanoparticles with an average size of 20 nm were uniformly riveted on the surface. Relevant studies show that CeO_2 nanoparticles riveted on the surface can increase the quality of graphene nanosheets and resist the agglomeration caused by van der Waals forces [36,37]. The high-resolution transmission electron microscopy (HRTEM) image in Fig. 2(f) is combined with FFT to show (200) and $(0\bar{1}1)$ lattice stripes with the crystal plane spacing of 0.28 nm. In addition, CeO_2 nanoparticles exhibit cubic shapes.

3.2. Properties of composite materials

As seen in Fig. 3(a), the hardness and conductivity of the CeO_2/GO-Cu30Cr0.2Zr composites are improved. For example, when the amount of CeO_2/GO is 0.3 wt%, the hardness and conductivity are increased by 26.9% and 33.7% respectively. As seen in Fig. 3(b), the tensile strength of the three composites is 276 MPa, 367 MPa, and 406 MPa respectively. The stress-strain curve of the CeO_2/GO-Cu30Cr0.2Zr composites shows an obvious yield stage. The addition of CeO_2/GO changes the failure mode from brittle fracture to plastic fracture. It can be seen from Fig. 3(c) that the maximum fracture elongation of the CeO_2/GO-Cu30Cr0.2Zr composites is increased twice. In addition, the toughness of the samples can be compared using the area under the stress-strain curve. The introduction of CeO_2/GO increases the plastic toughness of the material 5 times. At the same time, compared with Cu30Cr0.2Zr composites, the thermal conductivity of reinforced composites is increased by 68.3% and 60.9% respectively. Moreover, the coefficient of thermal expansion at 100 ℃ is significantly reduced, as seen in Fig. 3(d).

3.3. Material transfer and arc erosion morphology

Fig. 4 shows the change of contact mass after 5000 cycles at DC 25 V and 10–30 A. The electrodes of Cu30Cr0.2Zr contact material exhibit serious mass loss under any test conditions and the mass loss increases sharply with loading current. This indicates that the molten electrode material is separated from the electrode, which greatly reduces the service life of the contact. The material instability gradually increases under a high electrical current. The mass change of 0.3CeO_2/GO-Cu30Cr0.2Zr and 0.5CeO_2/GO-Cu30Cr0.2Zr composite materials is shown in Fig. 4(b) and (c). The cathode mass loss and anode net gain are observed between 10 A and 25 A applied current. The net transmission amount and

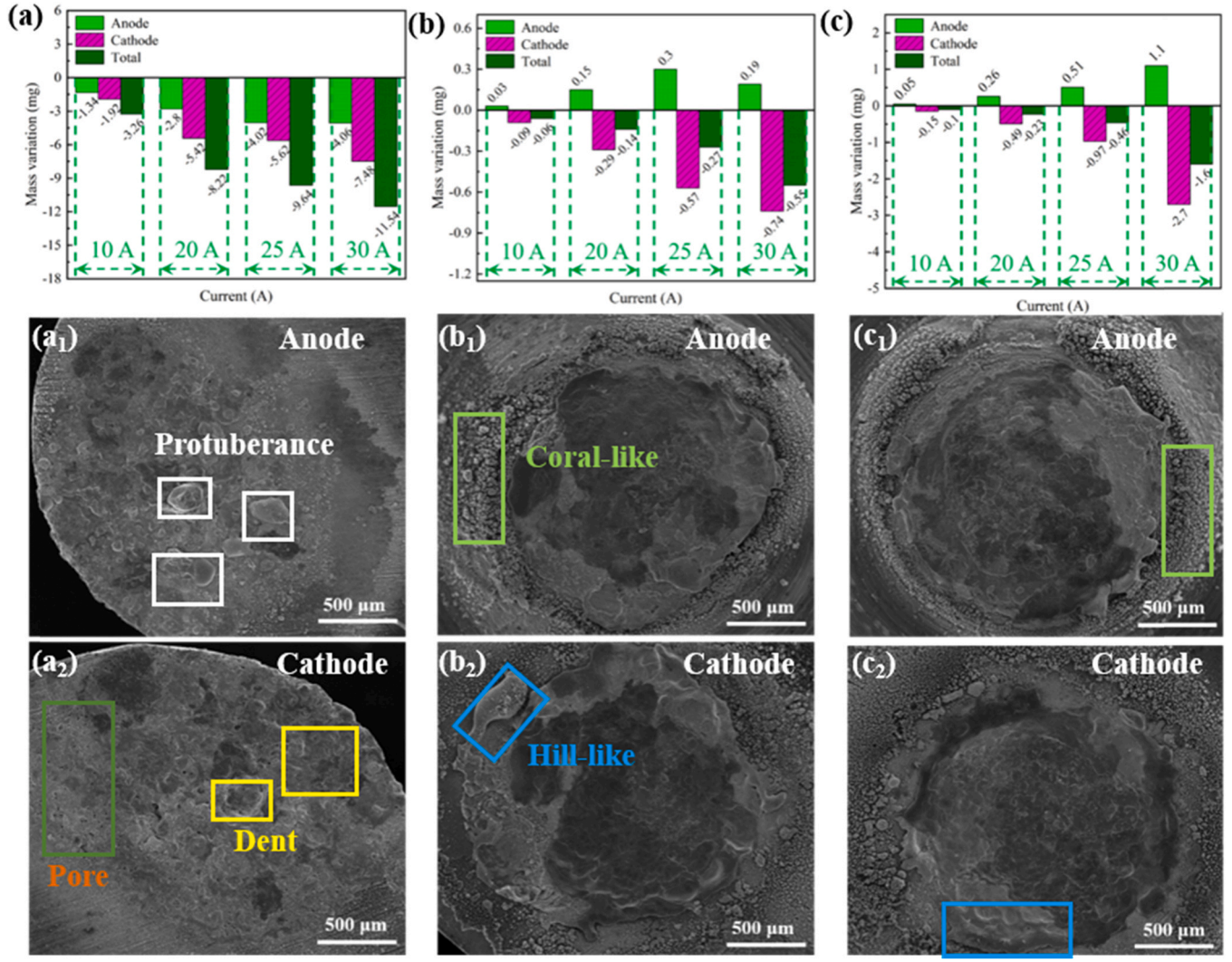

Fig. 4. Quality change and contact electrode ablation morphology before and after arc erosion: Mass transfer of (a-a_2) Cu30Cr0.2Zr, (b-b_2) 0.3CeO_2/GO-Cu30Cr0.2Zr and (c-c_2) 0.5CeO_2/GO-Cu30Cr0.2Zr.

transmission rate increase with the current. However, compared with 25 A, the anode mass gain rate decreases sharply at 30 A. According to Fig. 4, the trend of the total mass of the electrode change is negative. That is, the net gain of the anode is lower than the mass loss of the cathode, indicating that the electrode material diffuses into the surrounding environment. However, compared with the Cu30Cr0.2Zr composite, CeO_2/GO can effectively reduce the electrode mass loss. The main reason is that the electric and thermal conductivity of the material is poor, the arc heat cannot actively diffuse into the surrounding environment, and the continuous heat absorption of the electrode leads to the gasification and evaporation of the molten metal. Moreover, the density of CeO_2/GO is less than various metals, and the coating on the surface of the molten droplet increases the surface tension of the solution, preventing the splashing and evaporation of the molten metal. In a word, the mass transfer direction of the electrode is finally determined as a cathode to anode.

At 25 V DC, 20 A, and 5000 contact cycles, the low magnification morphology characteristics of arc erosion of cathode and anode contacts are seen in Fig. 4(a_1-c_2). The anode surface of Cu30Cr0.2Zr material has an obvious peak-like bulge. The main component of the bulge is identified as a copper-rich area, which contains no Cr. Correspondingly, the cathode is seriously eroded by the arc, with erosion pits of different sizes, and cluster pores at the edge, as seen in Fig. 4(a_1, a_2). There are no large bulges and ablation pits on the electrode surface of CeO_2/GO-Cu30Cr0.2Zr. The molten metal splashes on the contact surface under the action of current and pressure and then cools, forming fine, coral-like, and hill-like granular protrusions in Fig. 4(b_1-c_2). The microstructure of the contact surface was observed and studied at high magnification. In Fig. 5(a, b) the surface of the Cu30Cr0.2Zr electrode has cracks, holes, and craters after arc erosion. EDS results show that the ratio of Cu/Cr of the three structures is between 1:7 and 1:3, and the massive loss of copper indicates that it is greatly affected by arc heat and serious arc erosion has occurred. Moreover, the cooling rate of molten copper and chromium in the cooling process is very different, which is an important reason for the formation of hot cracks and other structures. After arc erosion, the surface microstructure of the CeO_2/GO-Cu30Cr0.2Zr electrode is mainly short rod-like, reticular-like, and plate skeleton, as seen in Fig. 5(c-f). After EDS identification, they have the same characteristics. The ratio of Cu/Cr/C is about 4:1:2. The three structures limit the flow and splashing of molten metal. Coral-like structures and particles have the same characteristics. The ratio of Cu/C/O is about 6:3:1, and the Cr element can be ignored.

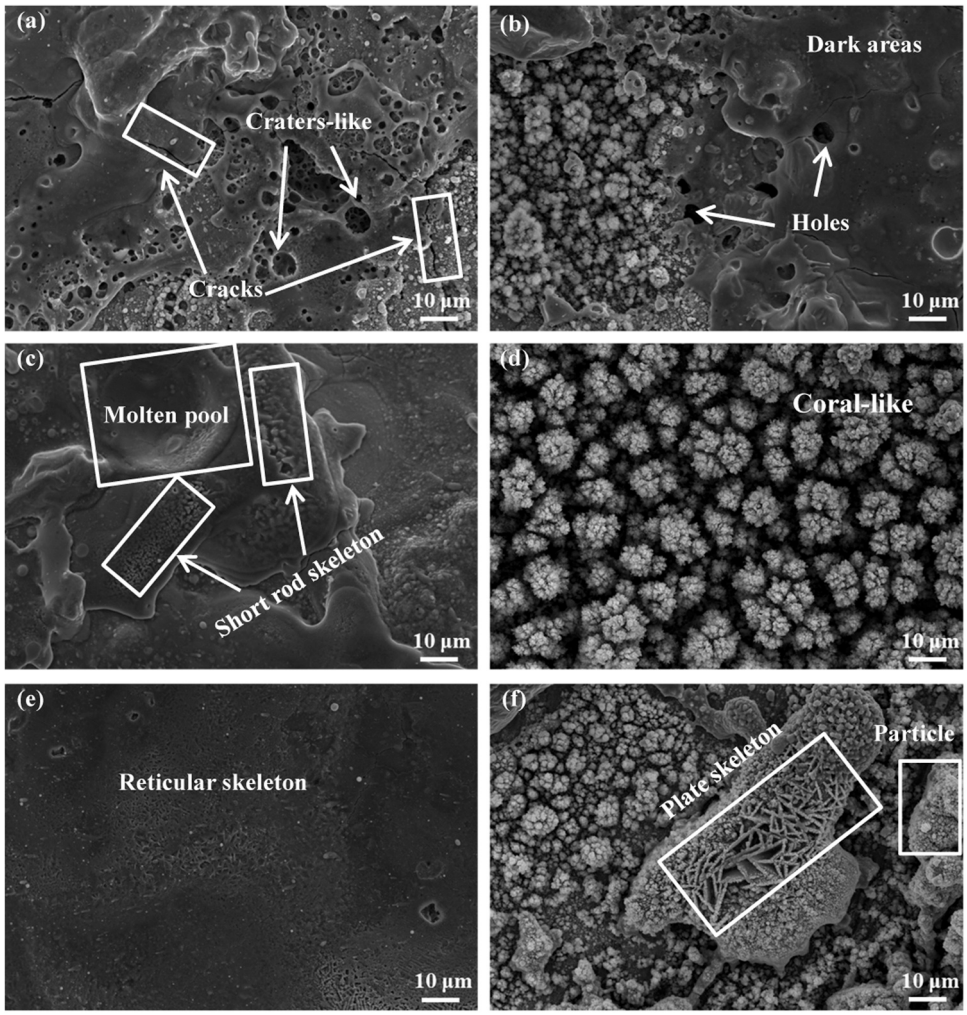

Fig. 5. Typical micromorphology of arc erosion: (a) Crater-like and cracks; (b) Holes and dark areas; (c) Short rod and molten pool; (d) Coral-like; (e) Reticular skeleton; (f) Plate skeleton and particle.

3.4. Microstructure analysis

Fig. S1-Fig. S3 shows the surface topography and element distribution of Cu30CrZr, 0.3CeO_2/GO-Cu30CrZr and 0.5CeO_2/GO-Cu30CrZr composites (Seeing in Supporting Information). As can be seen from Fig. S1- Fig. S3, the composite material is compact in structure, without obvious defects such as pores and particle agglomeration, and the elements are evenly distributed in the copper matrix.

In this section, 0.3CeO_2/GO-Cu30Cr0.2Zr composite is used as an example to show the representative TEM images of the sintered samples. As seen in Fig. 6(a), grain boundaries hinder the movement of a large number of dislocations, forming dislocation walls and dislocation packets. Fig. 6(b, c) show the twin morphology and selected area electron diffraction and determines that the crystal band axis is [$1\bar{1}0$]. It can be judged from Fig. 6(d) that the twin boundary is a stable coherent twin boundary, and the strain energy and interface energy are very low. Wang et al. [38] showed that the twin boundary has a great obstacle to the movement of dislocations, and it is easy to accumulate dislocations here and produce stress concentration. In addition, the twin interface energy is relatively low, which can absorb dislocations, and dislocations can slip at the twin boundary. This determines the important role of twins in improving mechanical strength and elongation. From the inverse fast Fourier transform (IFFT) diagram and geometric phase analysis (GPA) maps, it can be seen that there are high-density dislocation regions and low strain regions on both sides of the twin boundary, as seen in Fig. 6(e, f).

Fig. 7 shows the representative TEM microstructure of the CeO_2/GO-CuCrZr composites, where a clear structure of the interface is observed. There is a strong adhesion between rGO and the metal matrix. In addition, a small number of nanoparticles were found, which were identified as $Cu_{10}Zr_7$ and $Cr_{23}C_6$, respectively from FFT. Regardless of reinforcement, the lack of holes and cracks at the interface with the copper matrix means that a good mechanical interface is formed, as seen in Fig. 7(a). Fig. 7(b, c) show the diffraction spots and crystal planes of the $Cu_{10}Zr_7$ compound ($0\bar{2}3$), (132), and (115), resulting in three crystal planes spaced 0.27 nm, 0.27 nm, and 0.37 nm, respectively. In addition, the results in Fig. 7(d) display that along with the ($0\bar{2}3$) crystal plane, a large number of internal dislocations are observed due to lattice distortions. Fig. 7(f, g) present ($13\bar{1}$), ($2\bar{2}2$) and (311) diffraction spots and crystal faces of the $Cr_{23}C_6$ compound. Based on the sensitivity of geometric phase analysis (GPA) to small strain, it becomes an effective image processing technique for high-resolution TEM (HRTEM). Fig. 7(h) shows the GPA of Fig. 7(e), representing the positive strain in the ε_{xx}[$2\bar{2}2$] direction. In terms of the color reflection, most of CeO_2/GO shows red and yellow, while most of $Cr_{23}C_6$ shows a blue-green hue, and there is an obvious dividing line between the two phases. These results indicate that CeO_2/GO plays an important role in improving the mechanical properties of the CuCr composites with strong interfacial bonding for metal deformation.

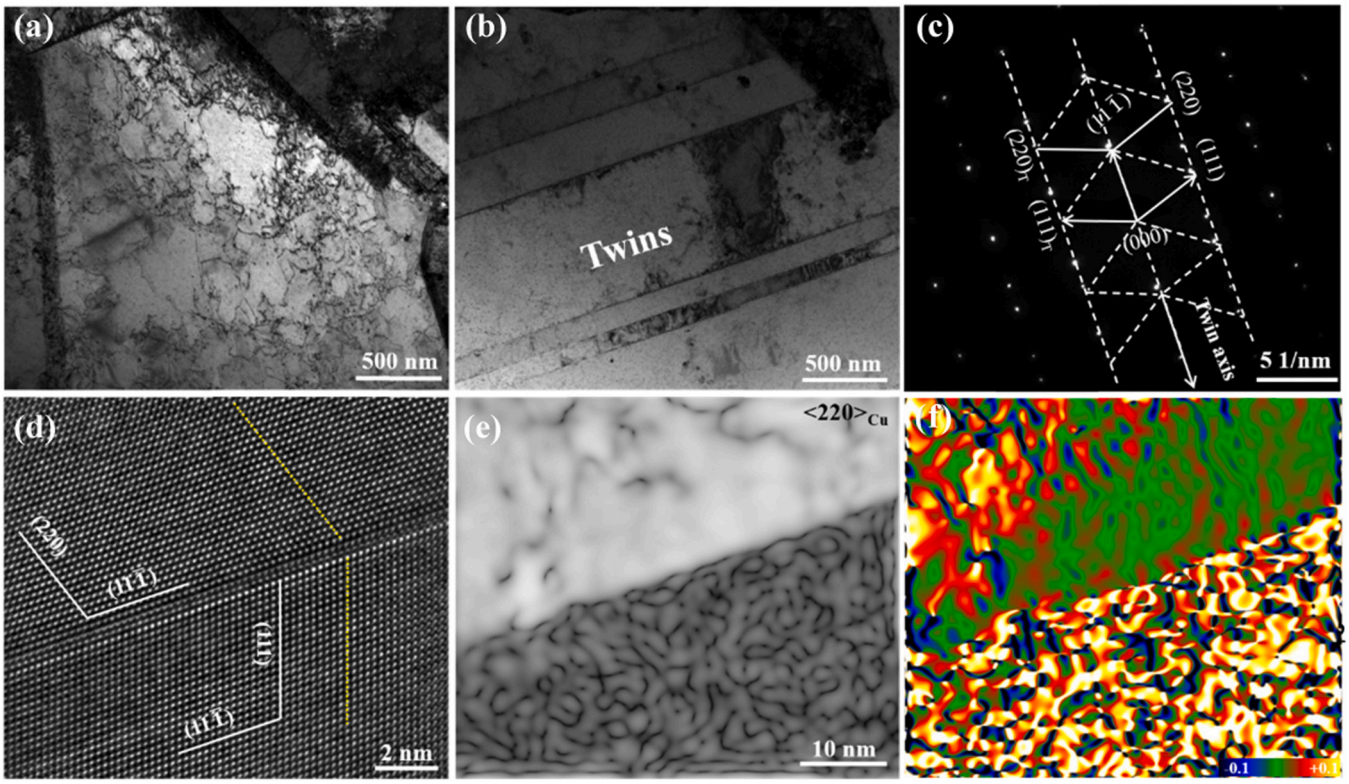

Fig. 6. (a) Dislocations distribution; (b) and (c) Twin morphology and small area electron diffraction pattern; (d) HRTEM of (b); (e, f) IFFT and GPA of (d).

4. Discussion

4.1. Strengthening mechanism analysis

At present, CeO_2/GO strengthens existing CuCr composites mainly in terms of electrical conductivity and mechanical strength. Given the strengthening effect, three possible mechanisms are discussed, including load redistribution, dislocation strengthening, and fine grain strengthening [3,39]:

$$\sigma_c = \sigma_m + \Delta\sigma_{Ds} + \Delta\sigma_{LRE} + \Delta\sigma_{FGs} \quad (1)$$

Here, σ_c and σ_m represent the tensile strength of the composite and the matrix, respectively. , $\Delta\sigma_{LRE}$ and $\Delta\sigma_{FGs}$ represent the contribution of dislocations, load redistribution, and fine grain strengthening to the tensile strength, respectively.

The large specific surface area and high aspect ratio of graphene determine that the load redistribution effect is the most important strengthening mechanism in graphene/metal composites [3]. Fig. 8 shows tensile fracture surfaces of the composite. The fracture surfaces of the Cu30Cr0.2Zr composite in Fig. 8(a, d) are full of gaps, and a large number of particles are pulled out from the matrix, presenting a loose interface structure, without obvious dimples and torn ridges. This means that due to weak interface bonding external load can cause the formation of holes at the interface and rapid crack growth and tear, greatly reducing the load transfer efficiency. In contrast, a large number of dimples were found on the whole fracture surface of the CeO_2/GO-Cu30Cr0.2Zr composite, which showed the characteristics of typical ductile fracture. In addition, Cr particles were firmly embedded in the Cu matrix, and no graphene was observed to be pulled out, but there was little or almost no gap at the interface junction. This indicates that CeO_2/GO acts as a bridge for interfacial bonding of the composites, establishing a strong interfacial bond and preventing or delaying the rapid propagation of cracks under high loads. In addition, the surface roughness of the fracture surface is 33.74 μm, 107.67 μm, and 91.47 μm respectively, calculated from the arithmetic average amplitude of the surface roughness fluctuations. There are significant differences in surface roughness between the three samples, indicating that graphene increases the total fracture surface area of the composite, and CeO_2/GO-Cu30Cr0.2Zr composite has a greater energy absorption capacity. Therefore, high load transfer efficiency is demonstrated by strong interface bonding.

The pinning effect of CeO_2/GO refines the grain size of the metal matrix. The grain structure was examined by electron backscatter diffraction (EBSD), as shown in Fig. 9. The average grain size of Cu30Cr0.2Zr and 0.5CeO_2/GO-Cu30Cr0.2Zr is 1.55 μm and 0.86 μm, respectively. The contribution of grain refinement was estimated using the Hall-Petch relationship [40]:

$$\Delta\sigma_g = kD^{-1/2} \quad (2)$$

$$D^{-1/2} = d_{RC}^{-1/2} - d_{UR}^{-1/2} \quad (3)$$

Here, k is the Hall-Petch coefficient (~0.071 MPa $m^{1/2}$ for Cu), and D is the average grain size of the matrix. The strength difference between the two samples due to grain refinement is estimated to be 19.4 MPa. It can be seen that the contribution of grain refinement to strength is not prominent or can be ignored. The main reason for the unchanged grain size is that SPS causes the metal powder to quickly bond and densify, which cannot provide enough time for grain size change, leading to the insignificant pinning effect of CeO_2/GO.

Finally, grain boundaries and graphene create barriers to dislocations movement in the metal matrix, leading to dislocation packing near the interface. As seen in Fig. 10(a, b), a large number of dislocations pileup at grain boundaries and form dislocation walls, thus an interface layer 80–120 nm thick is formed at the junction of rGO and the metal matrix. FFT images in Fig. 10(b), Inset A are identified as Cr_3C_2. Nanolayered carbides seriously hinder dislocation movement. The dislocation density can be quantitatively estimated by the XRD analysis of bulk samples based on the Williamson-Hall method [41,42]. XRD patterns of Cu30Cr0.2Zr and

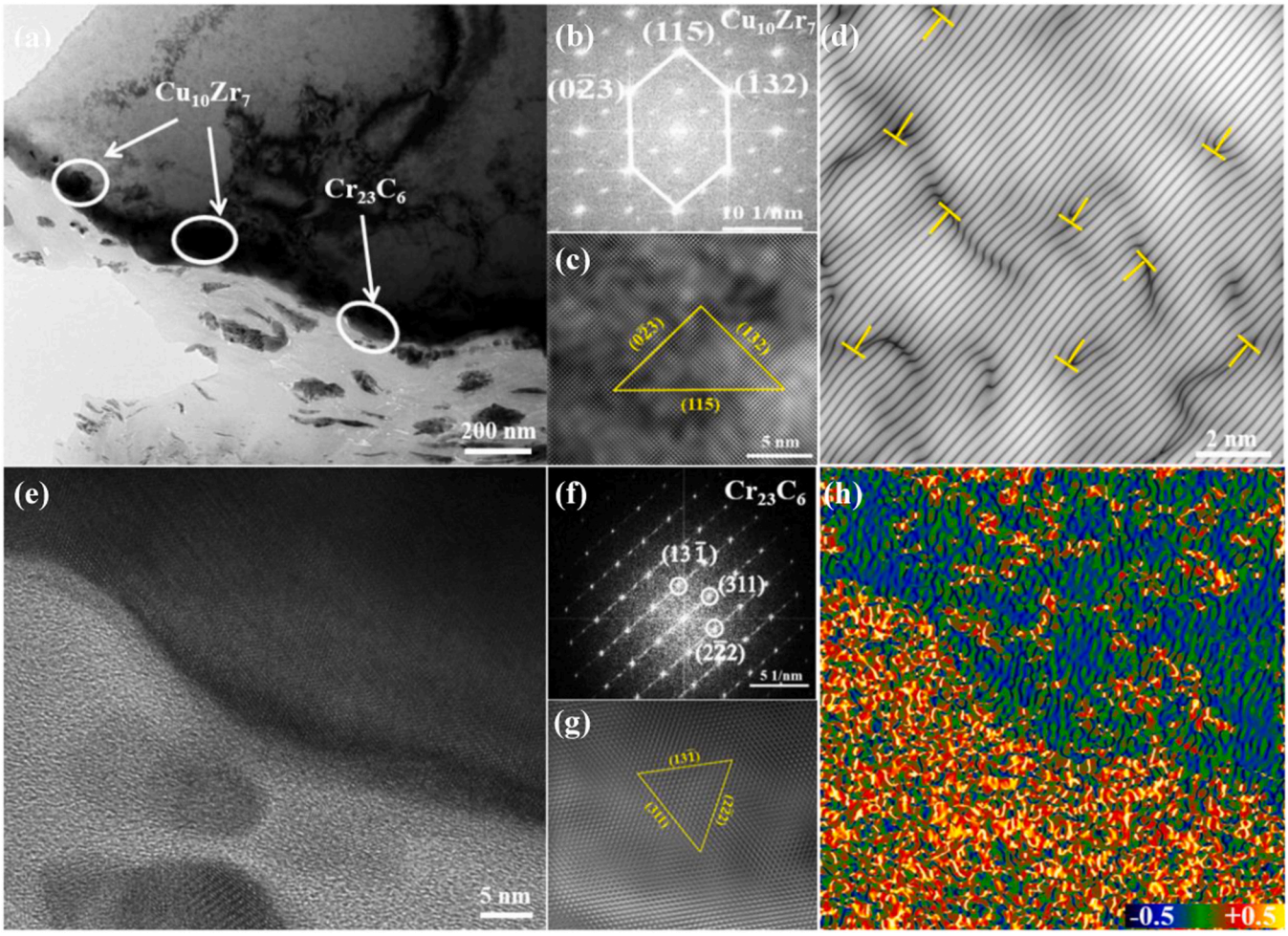

Fig. 7. Interface analysis. (a) TEM micrograph showing the rGO/CuCrZr interface; (b-d) FFT and IFFT images of $Cu_{10}Zr_7$ nanoparticles; (e) HRTEM of $Cr_{23}C_6$; (f, g) FFT and IFFT images of $Cr_{23}C_6$ nanoparticles; (h) GPA of (e).

0.3CeO_2/GO-Cu30Cr0.2Zr composites after tensile fracture are shown in Fig. 10(c). The strongest X-ray diffraction reflection comes from the $(111)_{Cu}$ planes, and all the reflections positions of the 0.3CeO_2/GO-Cu30Cr0.2Zr composite are blue-shifted compared with the Cu30Cr0.2Zr composite. The dislocation density (ρ) of the stretched sample is calculated as [41]:

$$\rho = \frac{2\sqrt{3}\,\varepsilon}{db} \tag{4}$$

Here, d, b, and ε are crystallite size, Burgers vector (0.256 nm [43]), and microstrain, respectively. d and ε can be determined by using the Williamson-Hall method [42], and according to the XRD results:

$$B\cos\theta = \frac{K\lambda}{d} + \sin\theta \tag{5}$$

Here, B is the full width at half maxima (FWHM) in radians, K is a constant (0.89), θ is Bragg's diffraction angle, and λ is the wavelength of X-ray (Cu K_α =0.154 nm).

According to the XRD patterns, B for the four reflections of (111), (200), (220), and (311) planes of the copper matrix can be determined. Eq. 5 is linearly fitted, and the values of d and ε can be extracted from the intercept and slope of the fitting line. By substituting the values of d and ε into Eq. 4, the dislocation density of 0.3CeO_2/GO-Cu30Cr0.2Zr and unenhanced Cu30Cr0.2Zr after tensile deformation is 8.04×10^{14} m^{-2} and 4.14×10^{14} m^{-2}, respectively. Similarly, the dislocation density of the 0.5CeO_2/GO-Cu30Cr0.2Zr composite after tensile deformation is 9.15×10^{14} m^{-2}. The dislocation density of the composites increases greatly after stretching, which indicates that the composite has a stronger dislocation hindrance due to the enhancement of interface bonding. The contribution of dislocation strengthening to strength improvement ($\Delta\sigma_D$) can be determined according to Arsenault et al. [44]:

$$\Delta\sigma_D = \Delta\sigma_{RC} - \Delta\sigma_{UC} = \alpha G b\left(\sqrt{\rho_R} - \sqrt{\rho_U}\right) \tag{6}$$

Here, $\Delta\sigma_{RC}$ and $\Delta\sigma_{UC}$ are the dislocation strengthening of CeO_2/GO reinforced and unreinforced composites after tensile deformation, respectively. α is the geometric constant (1.25 [44]), G is the shear modulus of the metal (42.1 GPa for Cu), ρ_R and ρ_U represent the dislocation density of CeO_2/GO reinforced and unreinforced composites, respectively. Therefore, according to Eq.6, $\Delta\sigma_D$ of the reinforced composites is 107 MPa and 133 MPa, respectively. Fig. 10(d) shows the contribution of various strengthening mechanisms.

In order to reveal the reasons for the improvement of electrical properties, X-ray photoelectron spectroscopy was used to characterize the chemical states and surface chemical structure changes of GO before and after sintering. As seen from Fig. 11(a), CeO_2/GO contains the same C and O elements as GO, and also has a visible Ce 3d peak, which means that high-purity CeO_2/GO is obtained. Fig. 11(b, c) show the XPS spectra of O 1 S. By comparison, CeO_2/GO has an obvious sharp peak at 529.4 eV, which is the characteristic peak of the O atom in CeO_2. Moreover, compared with the O 1 s spectrum of GO, the peak position of the O atom in CeO_2/GO has a blue shift. This is because when Ce combines with O, the

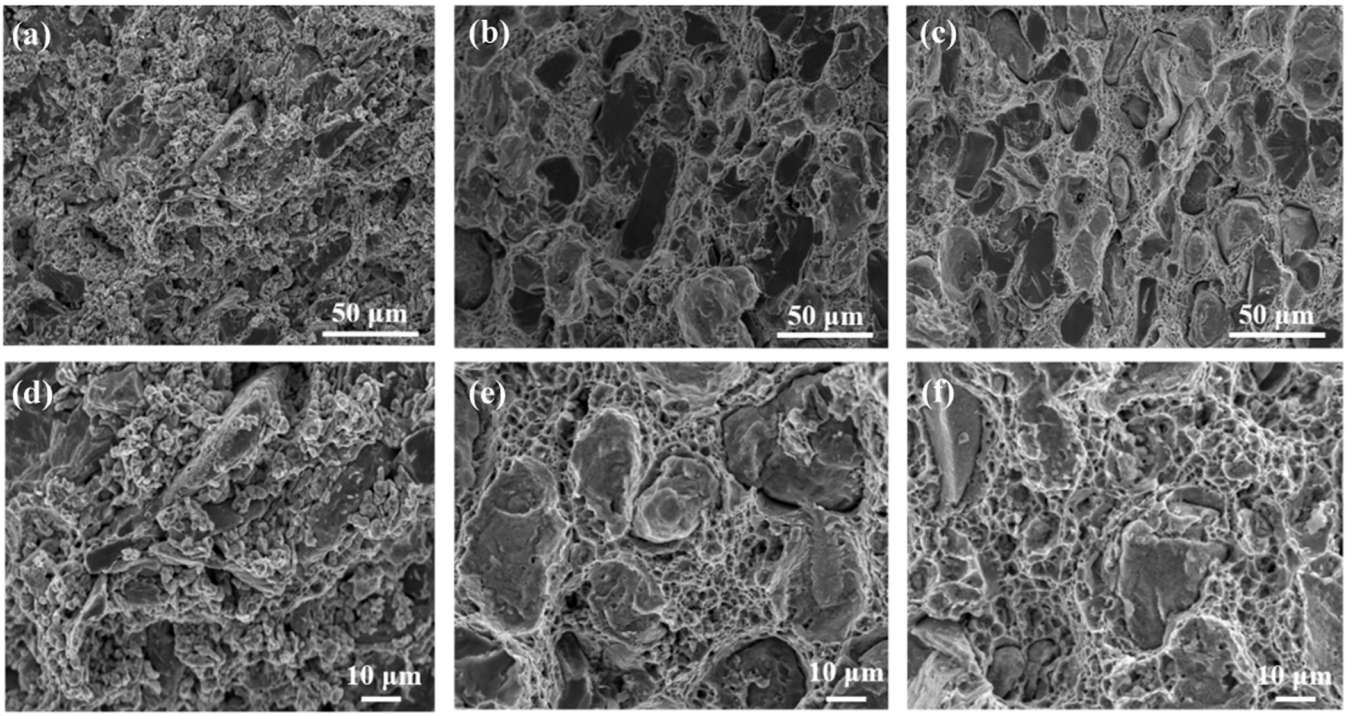

Fig. 8. (a, d) Low and high magnification fracture morphology of the CuCrZr composite; (b, c) Low and (e, f) high magnification fracture morphology of the CeO_2/GO-CuCrZr composite.

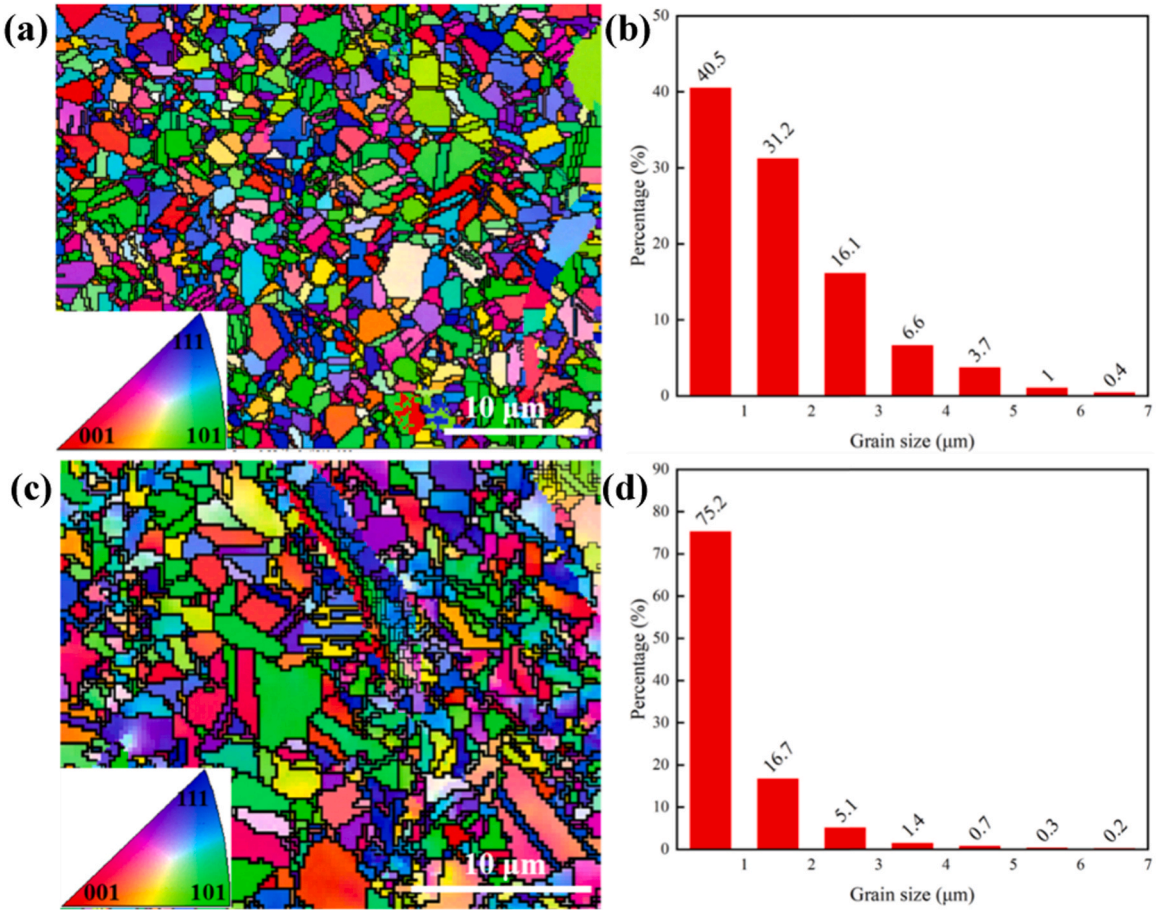

Fig. 9. EBSD diagram along the axial direction and the corresponding grain distribution. (a, b) CuCrZr; (c, d) CeO_2/GO-CuCrZr.

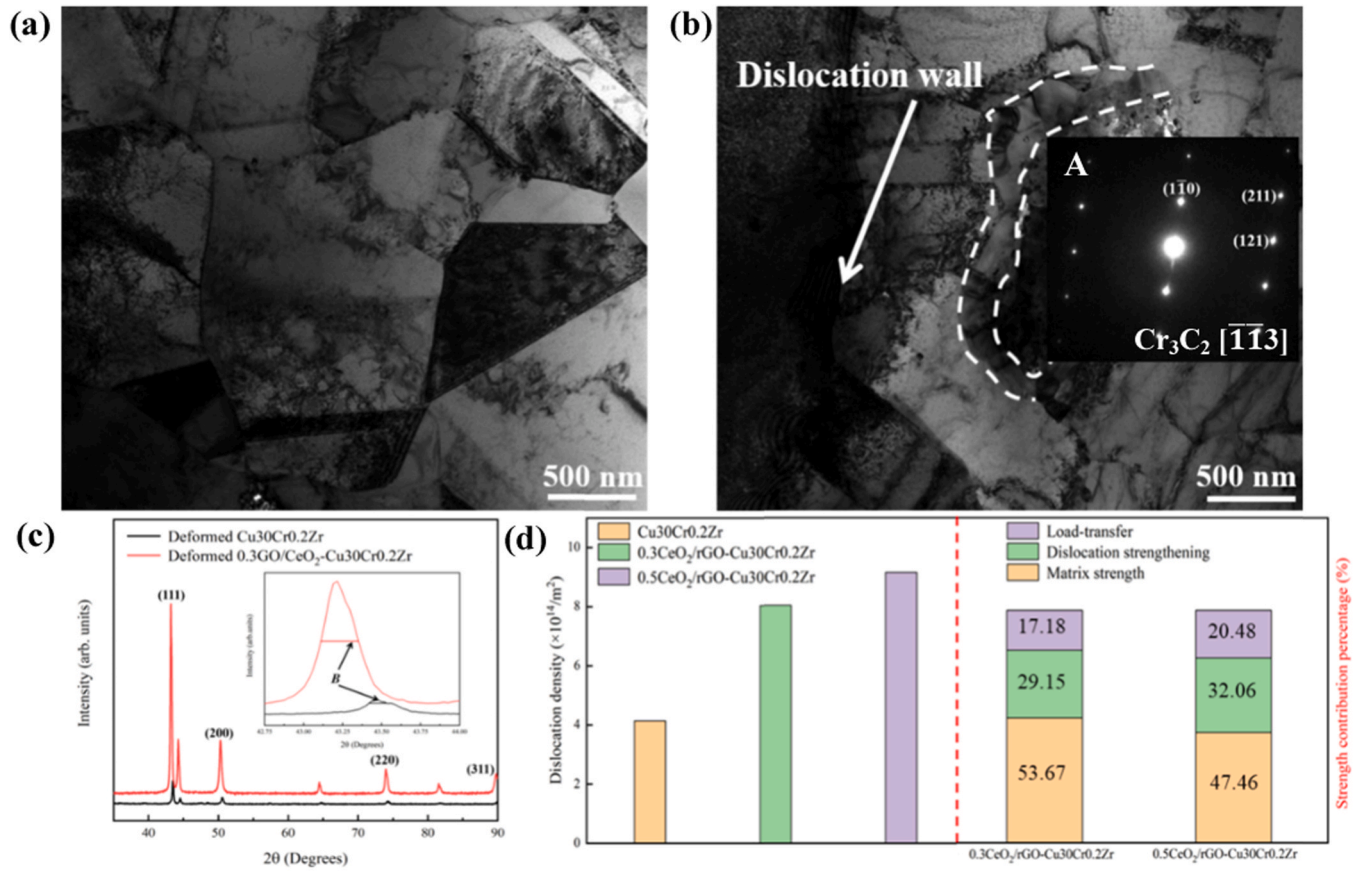

Fig. 10. (a, b) Distribution of dislocations; (c) XRD patterns of Cu30Cr0.2Zr and CeO_2/GO-CuCrZr composites after tensile deformation; (d) Dislocation density and reinforcement contribution rate after tensile test.

electronegativity of O is high, which causes the lone electron of Ce to shift its direction, increasing electron density, and thus shifting to the direction of lower binding energy. The C peaks of four different chemical valence states are displayed in the XPS spectra of C 1 S in Fig. 11(e-g). They mainly include hydroxyl (C-O), epoxy (O-C-O), carbonyl (O-C═O/C═O), and oxygen-free carbon ring (C-C/C═C). Through hydrothermal and high-temperature reduction, the peak strength of oxygen-containing groups decreases sharply, while the peak strength of the C-C/C═C bond increases significantly. Fig. 11(h) shows the statistics of the specific proportion of various functional groups. The content of oxygen-free carbon rings increases from 33.4% to 86.3% and 85.9%, respectively, and the content of oxygen-containing functional groups decreases from 66.6% to 13.7% and 14.1%, respectively. This result is consistent with the change of peak intensity, indicating that GO has completed the transformation to rGO. GO loses its excellent conductivity of graphene, due to a large number of functional groups on the surface. However, XPS results show that GO has recovered the excellent conductivity of graphene to a large extent, although the oxygen-containing functional groups have not been completely lost after sintering. On the other hand, CeO_2 nanoparticles have excellent ionic conductivity, which also improves the conductivity of composites to a certain extent.

In addition, the CuCrZr composite material without the addition of the reinforced phase, the interface binding capacity is insufficient, which increases the scattering effect of free electrons at the interface, relatively speaking, the CeO_2/GO-CuCrZr composite material has good interfacial binding performance, and the scattering effect on electrons is reduced.

4.2. Electrical contact characteristics

During use, the contact pair will gradually fail with the aggravation of arc erosion, and its failure modes include fusion welding and breakdown. In order to further explore the failure mechanisms of contact materials, this section discusses the relationship between fusion welding force, tensile strength, and arc burning energy. The fusion welding force can be expressed as in [45,46]:

$$K_{wt} = \frac{\varphi_e T_m \sqrt{C_V \rho \lambda}}{\varphi_i^2 \varphi_a} \tag{7}$$

$$F_m = KW^{2/3} \approx KW_A^{\frac{2}{3}} \tag{8}$$

Here, K_{wt} and F_m represent the welding tendency and the maximum welding force, respectively. The larger the value of K_{wt}, the better the welding resistance. φ_e and φ_a are the work functions of the anode and cathode contacts, respectively, and since the electrode materials are the same, the work function remains the same. T_m is the melting temperature, C_V is the specific heat, λ is the thermal conductivity. K and W represent the contact coefficient of the material and the total energy input by the electrode material, respectively. W includes arc heat and Joule heat. It is generally believed that the heat generated by the arc is much greater than the Joule heat. Therefore, the total energy input by the electrode is equal to the arc heat (W_A). The contact coefficient K is expressed as in [12]:

$$K = \Gamma\pi\left[\frac{3}{4\pi\delta[C_V(T_m - T_b)] + C_L}\right]^{2/3} \tag{9}$$

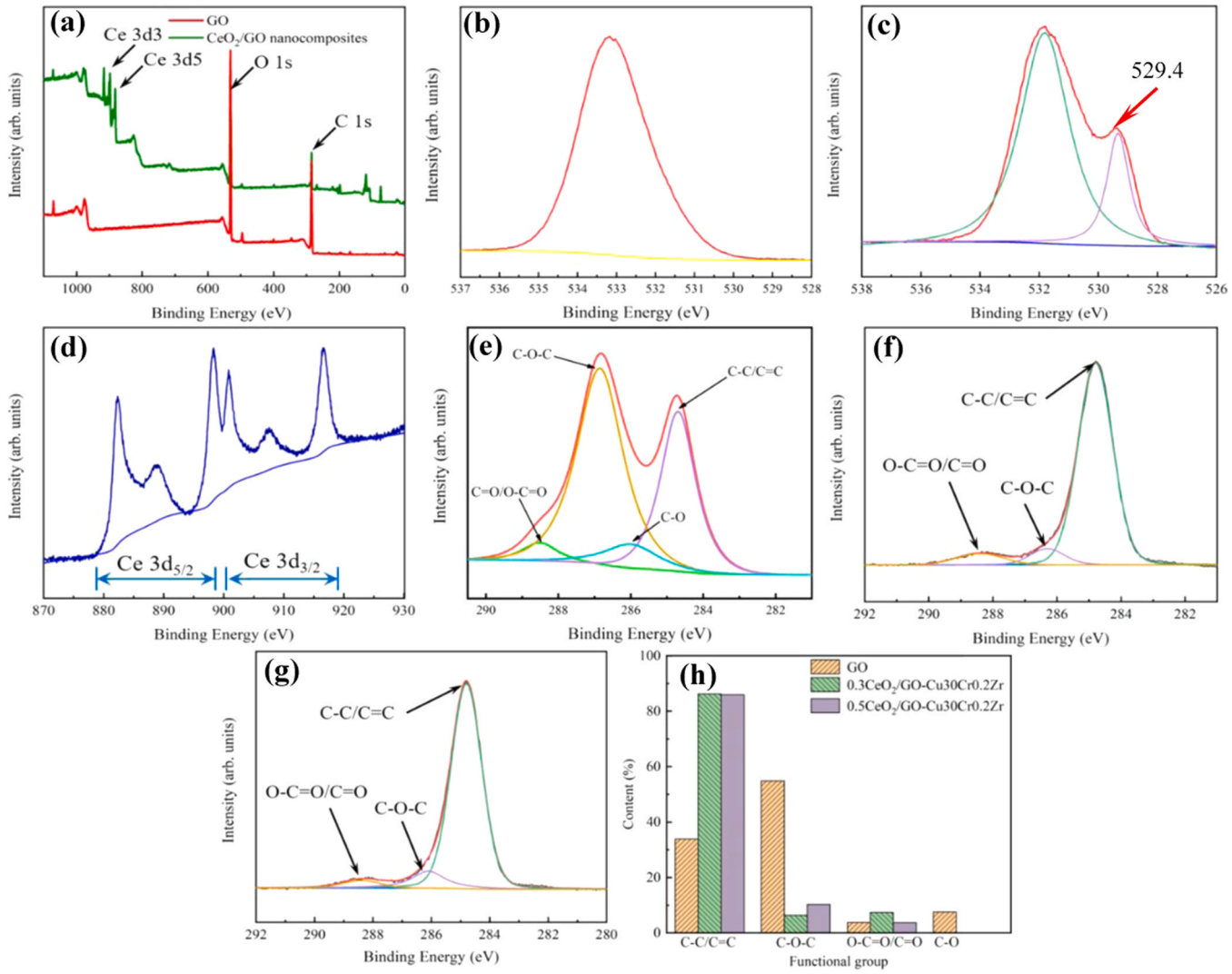

Fig. 11. XPS spectra analysis: (a) GO and CeO_2/GO; (b, c) O 1 s spectra of GO and CeO_2/GO; (d) Ce 3d; (e-g) C 1 s spectra of GO and composites in the sintered state; (h) proportion of functional groups.

Here, Γ and δ represent the tensile strength of the composite and the density of the molten material, respectively. T_b is the initial temperature and C_L is the melting latent heat of Cu. For the three composites, δ and C_V have no significant difference. Therefore, it can be seen from Eq. 9 that tensile strength and arc energy play an important role in controlling the value of the fusion welding force. Therefore, the expression of fusion welding force can be changed to:

$$F_m = C\Gamma W_A^{\ 2/3} \tag{10}$$

Here, C is a constant, and Γ of Cu30Cr0.2Zr and 0.5CeO_2/ GO-Cu30Cr0.2Zr is 276 MPa and 406 MPa, respectively. When the current is 30 A, W_A is 404 mJ and 67 mJ, respectively. The fusion welding force of Cu30Cr0.2Zr is 2 times that of 0.5CeO_2/GO-Cu30Cr0.2Zr, which shows that the theoretical calculation is consistent with the test results (0.593 N and 0.296 N). λ of unreinforced materials and 0.5CeO_2/ GO-Cu30Cr0.2Zr composites is 159.42 W/(m·k) and 264.9 W/(m·k), respectively. The calculation results of Eq. 7 show that CeO_2/GO increases the welding resistance of the composite, and these results are consistent with the fusion welding force.

5. Conclusions

(1) CeO_2/GO-Cu30Cr0.2Zr electrical contact material was successfully prepared by the hydrothermal method and SPS. In the sintering process, GO completed the transition to rGO, and CeO_2 improved the ionic conductivity, compared with Cu30Cr0.2Zr electrical contact material. The electrical conductivity increased by more than 30%, and the thermal conductivity increased by 68.3% and 60.9%, respectively.

(2) Amorphous carbon atoms generate $Cr_{23}C_6$ nanoparticles and Cr_3C_2 carbide layer in situ at the rGO-CuCrZr interface. In addition, a small number of nano-$Cu_{10}Zr_7$ compounds are formed in the matrix. All three contribute to the improvement of the CeO_2/GO-CuCrZr composites interface. At the same time, there is a distortion zone at the rGO-$Cr_{23}C_6$ interface, and the Cr_3C_2 carbide layer hinders the movement of a large number of dislocations. The tensile strength of reinforced Cu30Cr0.2Zr electrical contact material increased from 276 MPa to 367 MPa and 406 MPa, respectively, and the elongation at failure increased twice.

(3) CeO_2/GO not only increases the welding resistance but also reduces the arc energy. At the same time, the relationship between fusion welding force, tensile strength, and arc energy are determined. rGO, mesh and plate skeleton limit the splash of molten metal, reduce the mass loss of electrode material and improve the arc erosion resistance of Cu30Cr 0.2Zr electrical contact material. In addition, the mass transfer direction of electrode material is finally determined as a cathode to anode.

CRediT authorship contribution statement

Shengli Liang: Conceptualization, Methodology, Formal analysis. **Yunzhang Li :** Methodology, Formal analysis. **Yi Zhang:** Writing – review & editing, Funding acquisition. **Meng Zhou:** Resources, Project administration. **Shuang Liu:** Data curation, Formal analysis. **Xu Li:** Investigation. **Yongfeng Geng:** Formal analysis. **Baohong Tian:** Resources, Supervision. **Yanlin Jia:** Visualization. **Yong Liu:** Resources, Supervision. **Alex A. Volinsky:** Writing – review & editing.

Data availability

The data that has been used is confidential.

Declaration of Competing Interest

The authors declare that they have no known competing financial interests or personal relationships that could have appeared to influence the work reported in this paper.

Acknowledgments

This work was supported by the National Natural Science Foundation of China (52071134), the Natural Science Foundation of the Henan Province (202300410144), the Program for Innovative Research Team at the University of the Henan Province (22IRTSTHN001), China Postdoctoral Science Foundation (2021T140779) and Outstanding Talents Innovation Fund of the Henan Province (ZYQR201912164).

Appendix A. Supporting information

Supplementary data associated with this article can be found in the online version at doi:10.1016/j.jallcom.2022.167759.

References

[1] X. Gao, H.Y. Yue, E.J. Guo, S.L. Zhang, L.H. Yao, X.Y. Lin, B. Wang, E.H. Guan, Tribological properties of copper matrix composites reinforced with homogeneously dispersed graphene nanosheets, J. Mater. Sci. Technol. 34 (2018) 1925–1931.
[2] S.C. Shu, Q. Zhang, J. Ihde, Q.L. Yuan, W. Dai, M.L. Wu, D. Dan, K. Yang, B. Wang, C. Xue, H.B. Ma, X. Zhang, J.M. Han, X.Y. Chen, C.T. Lin, W.B. Ren, Y.F. Ma, N. Jiang, Surface modification on copper particles toward graphene reinforced copper matrix composites for electrical engineering application, J. Alloy Compd. 891 (2022) 162058.
[3] D.B. Xiong, M. Cao, Q. Guo, Z. Tan, G. Fan, Z. Li, D. Zhang, Graphene-and-copper artificial nacre fabricated by a preform impregnation process: bioinspired strategy for strengthening-toughening of metal matrix composite, ACS Nano 9 (2015) 6934–6943.
[4] N. Zhao, S. Guo, X. Zhang, C. He, C. Shi, Progress on graphene/copper composites focusing on reinforcement configuration design: a review, Acta Met. Sin. 57 (9) (2021) 1087–1106.
[5] M. Cao, D.B. Xiong, Z.Q. Tan, G. Ji, B. Amin-Ahmadi, Q. Guo, G.L. Fan, C.P. Guo, Z.Q. Li, D. Zhang, Aligning graphene in bulk copper: nacre-inspired nanolaminated architecture coupled with in-situ processing for enhanced mechanical properties and high electrical conductivity, Carbon 117 (2017) 65–74.
[6] H.R. Lin, X.H. Guo, K.X. Song, S.L. Li, J. Feng, X.F. Zhang, M.Q. Fen, Synergistic strengthening effect of tungsten carbide (WC) particles and silicon carbide whiskers (SiC_w) on mechanical properties of Cu-Al_2O_3 composite, J. Mater. Res Technol. 15 (2021) 2837–2847.
[7] X.H. Zhang, Y. Zhang, B.H. Tian, Y.L. Jia, M. Fu, Y. Liu, K.X. Song, A.A. Volinsky, X. Yang, H. Sun, Graphene oxide effects on the properties of Al_2O_3-Cu/35W5Cr composite, J. Mater. Sci. Technol. 37 (2020) 185–199.
[8] R. Nachiketa, K. Bernd, M. Timo, F. Ludo, V. Kim, V. Jef, Effect of WC particle size and Ag volume fraction on electrical contact resistance and thermal conductivity of Ag-WC contact materials, Mater. Des. 85 (2015) 412–422.
[9] H.J. Cao, Z.Q. Tan, G.L. Fan, Q. Guo, Y. Su, Z.Q. Li, D.B. Xiong, Wide and fine alignment control and interface modification for high-performance thermally conductive graphite/copper composite, Compos Part B-Eng. 191 (2020) 107965.
[10] H.R. Lin, X.H. Guo, K.X. Song, J. Feng, S.L. Li, X.F. Zhang, Synergistic strengthening mechanism of copper matrix composite reinforced with nano-Al_2O_3 particles and micro-SiC whiskers, Nanotechnol. Rev. 10 (1) (2021) 62–72.
[11] X.H. Zhang, Y. Zhang, B.H. Tian, J.C. An, Z. Zhao, A.A. Volinsky, Y. Liu, K.X. Song, Arc erosion behavior of the Al_2O_3-Cu/(W, Cr) electrical contacts, Compos Part B-Eng. 160 (2019) 110–118.
[12] F. Long, X.H. Guo, K.X. Song, S.G. Jia, V. Yakubov, S.L. Li, S.H. Liang, Enhanced arc erosion resistance of TiB_2/Cu composites reinforced with the carbon nanotube network structure, Mater. Des. 183 (2019) 108136.
[13] Z.R. Hu, R. Dai, D.N. Wang, X.N. Wang, F. Chen, X.L. Fan, C.J. Chen, Y.L. Liao, Q. Nian, Preparation of graphene/copper nanocomposites by ball milling followed by pressureless vacuum sintering, N. Carbon Mater. 36 (2) (2021) 420–428.
[14] J. Ding, W.B. Tian, P. Zhang, M. Zhang, Y.M. Zhang, Z.M. Sun, Arc erosion behavior of Ag/Ti_3AlC_2 electrical contact materials, J. Alloy Compd. 740 (2018) 669–676.
[15] C.P. Wu, D.P. Yi, W. Weng, S.H. Li, J.M. Zhou, F. Zheng, Arc erosion behavior of Ag/Ni electrical contact materials, Mater. Des. 85 (2015) 511–519.
[16] X.M. Duan, M.R. Wang, D.C. Jia, N. Jing, Z.L. Wu, Z.H. Yang, Z. Tian, S.J. Wang, P.G. He, Y.J. Wang, Y. Zhou, Anisotropic mechanical properties and fracture mechanisms of textured h-BN composite ceramics, Mater. Sci. Eng. A 607 (23) (2014) 38–43.
[17] X.Y. Zhang, Z.Q. Shi, X. Zhang, K. Wang, Y.Y. Zhao, H.Y. Xia, J.P. Wang, Three dimensional AlN skeleton-reinforced highly oriented graphite flake composites with excellent mechanical and thermophysical properties, Carbon 131 (2018) 94–101.
[18] A.A. Balandin, S. Ghosh, W. Bao, I. Calizo, D. Teweldebrhan, F. Miao, C.N. Lau, Superior thermal conductivity of single-layer graphene, Nano Lett. 8 (3) (2008) 902–907.
[19] D.L. Nika, S. Ghosh, E.P. Pokatilov, A.A. Balandin, Lattice thermal conductivity of graphene flakes: comparison with bulk graphite, Appl. Phys. Lett. 94 (20) (2009) 203103.
[20] K.I. Bolotin, K. Sikes, Z. Jiang, M. Klima, G. Fudenberg, J. Hone, P. Kim, H. Stormer, Ultrahigh electron mobility in suspended graphene, Solid State Commun. 146 (9) (2008) 351–355.
[21] H. Chen, M.B. Müller, K.J. Gilmore, G.G. Wallace, D. Li, Mechanically strong,-electrically conductive, and biocompatible graphene paper, Adv. Mater. 20 (18) (2008) 3557–3561.
[22] C. Lee, X. Wei, J.W. Kysar, J. Hone, Measurement of the elastic properties andintrinsic strength of monolayer graphene, Science 321 (5887) (2008) 385–388.
[23] X. Zhang, C.S. Shi, E.Z. Liu, F. He, L.Y. Ma, Q.Y. Li, J.J. Li, W. Bacsa, N.Q. Zhao, C.N. He, Achieving high strength and high ductility in metal matrix composites reinforced with a discontinuous three-dimensional graphene-like network, Nanoscale 9 (33) (2017) 11929–11938.
[24] S. Zhao, Z. Zheng, Z. Huang, S. Dong, P. Luo, Z. Zhang, Y.W. Wang, Cu matrix composites reinforced with aligned carbon nanotubes: mechanical, electrical and thermal properties, Mater. Sci. Eng. A 675 (2016) 82–91.
[25] H. Wang, Z.H. Zhang, Z.Y. Hu, F.C. Wang, S.L. Li, E. Korznikov, X.C. Zhao, Y. Liu, Z.F. Liu, Z. Kang, Synergistic strengthening effect of nanocrystalline copper reinforced with carbon nanotubes, Sci. Rep. 6 (2016) 26258.
[26] X. Zhang, N.Q. Zhao, C.N. He, The superior mechanical and physical properties of nanocarbon reinforced bulk composites achieved by architecture design-A review, Prog. Mater. Sci. 113 (2020) 100672.
[27] X. Zhang, Y.X. Xu, M.C. Wang, E.Z. Liu, N.Q. Zhao, C.S. Shi, D. Lin, F.L. Zhu, C.N. He, A powder-metallurgy-based strategy toward three-dimensional graphene-like network for reinforcing copper matrix composites, Nat. Commun. 11 (2020) 1–13.
[28] X. Zhang, D.Q. Wan, K. Peng, W. Zhang, Enhancement of thermal conductivity and mechanical properties of Cu-reduced graphene oxide composites by interface modification, J. Mater. Eng. Perform. 28 (8) (2019) 5165–5171.
[29] L.D. Wang, Z.Y. Yang, Y. Cui, B. Wei, S.H. Xu, J. Sheng, M. Wang, Y.P. Zhu, W.D. Fei, Graphene-copper composite with micro-layered grains and ultrahigh strength, Sci. Rep. 7 (1) (2017) 2558–2561.
[30] X.Y. Si, M. Lia, F.Y. Chen, P. Eklundd, J.M. Xue, F. Huang, S.Y. Du, Q. Huang, Effect of carbide interlayers on the microstructure and properties of graphene-nanoplatelet-reinforced copper matrix composites, Mat. Sci. Eng. A 708 (21) (2017) 311–318.
[31] K. Chu, F. Wang, Y.B. Li, X.H. Wang, D.J. Huang, H. Zhang, Interface structure and strengthening behavior of graphene/CuCr composites, Carbon 133 (2018) 127–139.
[32] Q. Liu, X. He, S. Ren, T. Liu, Q. Kang, X. Qu, Effect of titanium carbide coating on the microstructure and thermal conductivity of short graphite fiber/copper composites, J. Mater. Sci. 48 (17) (2013) 5810–5817.
[33] X. Zhang, Y.X. Xu, M.C. Wang, E.Z. Liu, N.Q. Zhao, C.S. Shi, D. Lin, F.L. Zhu, C.N. He, A powder-metallurgy-based strategy toward three-dimensional graphene-like network for reinforcing copper matrix composites, Nat. Commun. 11 (2020) 2775.
[34] S. Stankovich, R.D. Piner, X.Q. Chen, N.Q. Wu, S.T. Nguyen, R.S. Ruoff, Stable aqueous dispersions of graphitic nanoplatelets via the reduction of exfoliated graphite oxide in the presence of poly (sodium 4-styrenesulfonate), J. Mater. Chem. 16 (29) (2006) 155–168.
[35] W.S. Hummers, R.E. Offeman, J. Am, Preparation of graphitic oxide, Chem. Soc. 80 (1958) 1339.
[36] L.H. Jiang, M.G. Yao, B. Liu, Q.J. Li, R. Liu, H. Lv, S.C. Lu, C. Gong, B. Zou, T. Cui, B.B. Liu, G. Hu, T. Wagberg, Controlled synthesis of CeO_2/graphene nanocomposites with highly enhanced optical and catalytic properties, J. Phy Che C. 116 (21) (2012) 11741–11745.

[37] C.Y. Min, Z.B. He, D.D. Liu, W. Jia, J.M. Qian, Y.H. Jin, S.J. Song, Ceria/reduced graphene oxide nanocomposite: synthesis, characterization, and its lubrication application, Chemistryselect 4 (15) (2019) 4615–4623.
[38] Z.J. Wang, Q.J. Li, Y. Li, L.C. Huang, L. Lu, M. Dao, J. Li, E. Ma, S. Suresh, Z.W. Shan, Sliding of coherent twin boundaries, Nat. Commun. 8 (2017) 1108.
[39] A. Nieto, A. Bisht, D. Lahiri, C. Zhang, A. Agarwal, Graphene reinforced metal and ceramic matrix composites: a review, Int Mater. Rev. 62 (2016) 241–302.
[40] N. Hansen, Hall-Petch relation and boundary strengthening, Scr. Mater. 51 (2004) 801–806.
[41] R.E. Smallman, K.H. Westmacott, Stacking faults in face-centered cubic metals and alloys, Philos. Mag. 2 (1957) 669–683.
[42] G.K. Williamson, R.E. Smallman, The use of Fourier analysis in the interpretation of X-ray line broadening from cold-worked iron and molybdenum, Acta Cryst. 7 (1954) 574–581.
[43] W. Kim, T. Lee, S. Han, Multi-layer graphene/copper composites: preparation using high-ratio differential speed rolling, microstructure and mechanical properties, Carbon 69 (2014) 55–65.
[44] R.J. Arsenault, N. Shi, Dislocation generation due to differences between the coefficients of thermal expansion, Mater. Sci. Eng. 81 (1986) 175–187.
[45] X.J. Liu, Analysis of welding mechanism on electrical contact of switches, LowVoltage Appar. (2006) 11–14.
[46] S.L. Liang, S. Liu, Y. Zhang, M. Zhou, B.H. Tian, Y.F. Geng, Y. Liu, Y.L. Jia, X. Li, A.A. Volinsky, Effect of in situ graphene-doped nano-CeO_2 on microstructure and electrical contact properties of Cu30Cr10W contacts, Nanotechnol. Rev. 10 (2021) 385–400.